Targeting spectral signatures of progressively dysplastic stratified epithelia using angularly variable fiber geometry in reflectance Monte Carlo simulations

Adrien Wang
Vengadesan Nammalavar
Rebekah Drezek
Rice University
Department of Bioengineering
Houston, Texas 77251-1892
E-mail: drezek@rice.edu

Abstract. A key component of accurate spectroscopic-based cancer diagnostics is the ability to differentiate spectral variations resulting from epithelial tissue dysplasia. Such measurement may be enhanced by discretely probing the optical properties of the epithelial tissue where the morphological and biochemical features vary according to tissue depths. More precisely, layer-specific changes in tissue optical properties correlated to cellular dysplasia can be determined by conventional reflectance spectroscopy when it is coupled with angularly variable fiber geometry. Thus, this study addresses how angularly variable fiber geometry can resolve spatially specific spectral signatures of tissue pathology by interpreting and analyzing the reflectance spectra of increasingly dysplastic epithelial tissue in reflectance-mode Monte Carlo simulation. Specifically, by increasing the obliquity of the collection fibers from 0 to 40 deg in the direction facing toward the illumination fiber, the spectral sensitivity to tissue abnormalities in the epithelial layer is thereby improved, whereas orthogonal fibers are more sensitive to the changes in the stromal layer. © *2007 Society of Photo-Optical Instrumentation Engineers.* [DOI: 10.1117/1.2769328]

Keywords: fiber optic probes; reflectance spectroscopy; epithelial tissue; Monte Carlo.

Paper 06323RR received Nov. 9, 2006; revised manuscript received Apr. 2, 2007; accepted for publication Apr. 14, 2007; published online Aug. 13, 2007.

1 Introduction

Optical spectroscopy has been used to characterize morphological, structural, and biochemical changes in cells and tissue. In particular, the potential utility of reflectance spectroscopy for the early detection of tissue malignancy has been previously demonstrated.[1–4] Examination of epithelial tissue reveals the developmental status of human carcinoma. Therefore, it is advantageous to probe this superficial tissue where intraepithelial dysplasia can be characterized by: 1. an increased nuclear-to-cytoplasmic ratio, and 2. the presence of hyperchromasia and pleomorphism.[2,5] Reflectance spectroscopy is minimally invasive and yields diagnostically valuable information about the sizes and distributions of scattering entities embedded in tissue (e.g., nuclei and intracellular organelles).[2,3,6–9] Although the diagnostic accuracy of optical techniques has been extensively investigated in many preliminary studies,[10–14] there is a compelling need to refine the tissue-depth selectivity of spectroscopic techniques to enhance their diagnostic sensitivity and specificity.

Depth-resolved, or depth-selective, reflectance spectroscopy has been approached from many perspectives. For example, polarized reflectance spectroscopy can be used to better isolate epithelial scattering from bulk reflectance measurements by selectively collecting reemitted light of the same polarization as the source.[3,15,16] Another approach involves varying the geometrical configurations of photon delivery and collection such that the result affects source-detector separation distances (SDSD),[17–19] aperture sizes,[20–24] angular numerical apertures,[20,22,25] the spacing between the distal tip of a probe and tissue surface,[20,21,26,27] or a probe's angular orientation with respect to the target tissue.[28,29] The objective of these geometrical manipulations is to differentiate low-order scattering in superficial tissue from photons diffusely scattered at deeper tissue depths. By selectively enhancing and minimizing photon collections from the target and background regions, respectively, depth-resolved optical spectroscopy can be achieved.

The geometrical configurations of photon delivery and collection, as noted before, can be achieved by using fiber optics via mechanical means, such as adjustable positioning and orientation of optical fibers in a fiber probe, or alternatively, via optical means, such as ray guidance using optical elements. Computational modeling and experimentation on tissue phantoms have been the basis for the design and optimization of fiber probe geometry for depth-resolved reflectance and fluorescence spectroscopy. Recently published studies supply some examples of this technology, and these include the following: Zhu, Liu, and Ramanujam,[22] who adopted a multi-separation fiber probe to achieve depth-selectable optical probing in breast tissue; Skala et al.,[30] who, in their Monte

Address all correspondence to Rebekah Drezek Bioengineering, Rice University, PO Box 1892, MS-142 - 6100 Main Street, Houston, TX 77005 United States of America; Tel: 713–348–3011; Fax: 713–348–5877 E-mail: drezek@rice.edu

Carlo study, showed that the fluorescence sensitivity to the epithelial layer dramatically improved from 15 to 72% at a source-detector separation of 200 μm when the illumination angle, measured out of the plane of tissue surface, increased from 0 deg (orthogonal) to 45 deg; and Nieman et al.[28] and Schwarz et al.,[31] who later showed that the same angular fiber approaches can result in depth selection in layered phantoms. Our previous study[29] involving the concept of angled fiber geometry also provided both a quantitative and systematic understanding about the efficacy of applying fiber geometry to reflectance measurements in biologically relevant environments. Specifically, we discovered that the collection fiber angles can be utilized to manipulate depth selection in tissue where probing depths are controlled by the orientation of the collection fibers with respect to the illumination axis. For example, more superficially probing depths can be achieved where collection fibers are facing toward the illumination point, the level depending on the degree of fiber rotation. On the other hand, collection fibers rotated away from the illumination point yield much more extensive probing depths into the basal layer of tissue at a given source-detector separation due to the exclusion of superficially scattered rays. All of these recent studies have contributed to a growing interest in the utility of using angularly variable fiber geometry to directly achieve depth selection in tissue.

While there is strong evidence to support the use of angled fiber geometry to achieve the desired layer selection, we believe that it is even more important to gain further understanding about the ability of using these proposed concepts to detect specific changes in tissue properties, because tissue properties, primarily those involving absorption and scattering due to alterations in tissue biochemistry and morphology, are important indicators of tissue pathology. It is precisely the central focus of this study to determine if the proposed fiber geometries can effectively detect and reveal changes in tissue properties by means of reflectance spectroscopy. Our previous effort specifically investigated the spatial distribution of scattered photons in a two-layer epithelial model at a single wavelength. Building on this foundation, the present study undertakes spectral analyses of the reflectance spectra gathered using different angular configurations of the collection fibers. We believe that such spectral analysis is necessary, because our previous study on depth-resolved reflectance does not provide sufficiently comprehensive information about the capability of spatially resolving reflectance spectra using angled fiber geometry. This is important because the spectral dependence of tissue reflectance is sensitive to the morphology of epithelial cells. In this study, we specifically focus on the quantitative changes in spectral fluence and structure when layered-specific tissue optical properties are varied in a two-layer tissue model. These properties consist of the parameters of scattering and absorption coefficients that collectively describe the general optical properties of human uterine-cervical epithelial tissue. In addition, we note that these tissue optical properties are precisely controlled in the simulation model. Consequently, the resulting quantitative data can be interpreted more easily than those derived from phantom-based experiments. Thus, the results and conclusions presented in this study may serve as a theoretical foundation on which to base future experimental studies.
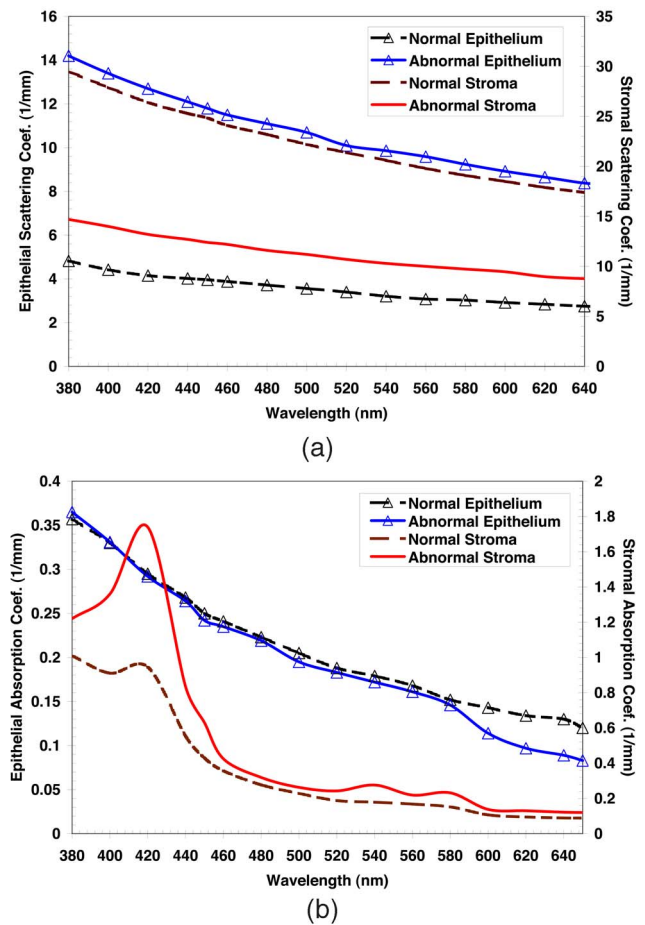

(a)

(b)

Fig. 1 (a) and (b) Optical properties of the normal and abnormal epithelial models are shown. The sectioned lines denote the properties of normal tissue; the triangular markers denote the epithelia and should be referenced to the primary axis on the left.

2 Methods

2.1 Tissue Model and Optical Properties

A two-layer cylindrical tissue model is used to represent human uterine-cervical epithelial tissue. The thickness of the epithelial (top) layer is set at 450 μm to approximate the average thickness of the human uterine-cervical epithelium.[32] The basal stromal layer is set at 10 mm, which is representative of a semi-infinite tissue layer underneath the epithelium. The cylindrical diameter of 20 mm is wide enough to encompass all photon paths collectible by our particular fiber geometries. The optical properties of the tissue model are based on the values reported by Collier et al.,[33] Chang et al.,[34] and Drezek et al.[3] that were also adopted by Zhu, Liu, and Ramanujam,[22] Wang et al.,[29] and Skala et al.[30] in their respective studies on epithelial tissue. The adopted scattering and absorption coefficients for the tissue model can be found in Figs. 1(a) and 1(b), respectively. The anisotropy factors of the epithelium and stroma are 0.94 and 0.89, respectively, and are assumed to be constant according to our references.[3,34]

2.2 Tissue Properties and Rationale

This study investigates the sensitivities of fiber probes to: 1. changes in tissue scattering properties and 2. changes in tissue

absorption. As previously noted, epithelial dysplasia is linked to the growth of epithelial nuclei and the consequent increase of scattering. To explain, in human stratified epithelial tissue, a typical nucleus has a diameter of approximately 5 μm, while the size can nearly double in cellular dysplasia. Cases involving an increase as large as 20 μm in diameter have been reported.[2,28,35–39] These enlarged nuclei in the epithelial layer consequently increase the local scattering coefficients of the affected region. However, in advanced neoplasm, where degradation of collagen occurs in the stromal layer,[40–42] a decrease in basal layer scattering has also been reported.[43,44] More importantly, such changes in tissue scattering result in differences in reflectance spectra, affecting detection of tissue pathology. Thus, the sensitivity and specificity of optical diagnostics applied to tissue may be enhanced where a given fiber geometry is able to identify the origins of detected spectra. From the perspective of tissue pathology then, it is important to understand how varying scattering properties of both epithelial and stromal layers may be better diagnosed with the angled fiber approach.

Three scattering scenarios are implemented in our tissue model. These scenarios take into account the development of tissue pathology relative to: 1. individual variations of the scattering coefficients of either the superficial or basal layer, and 2. simultaneous changes of tissue scattering in both layers. We use the scattering coefficients of the normal and abnormal cervical tissue as the boundary values of our model. Between these boundaries, three intermediate and equidistant points are designated as the transitional stages of tissue dysplasia. The scattering coefficients of the normal and abnormal tissue corresponding to both epithelial and stromal layers are shown in Fig. 1(a). The three intermediate levels are omitted from the graph to avoid cluttering, but those values can be calculated as the weighted means (25/75, 50/50, and 75/25 percentage ratios) of the boundary values. This model does assume that the correlation between tissue pathology and scattering is linearly proportional. However, we believe it is justified in this particular study, since our primary aim focuses on investigating the capability of various fiber designs to differentiate, among reflectance spectra, the changes in layer-specific tissue properties. To emphasize the effect of tissue scattering, we keep the absorption coefficients of the tissue model constant and equal to those of the normal epithelial tissue.

With regard to tissue absorption, hemoglobin is perhaps the most dominant and relevant tissue chromophore. As such, accelerated metabolism and neovascularization associated with tissue neoplasia significantly affect the level of hemoglobin absorption in tissue;[45–47] therefore, hemoglobin absorption is an important indicator of tissue pathology. However, it is generally believed that neovascularization usually does not appear at the onset of epithelial dysplasia, during which period most observable abnormalities are manifested in the epithelial layer. In addition, general hemoglobin absorption can pose a significant interference to the measurement of other physiological parameters, such as intrinsic tissue fluorescence and absorption due to nonhemoglobin chromophores. Notwithstanding these complications, our objective focuses on the performance of angular fiber geometry with respect to tissue absorption at different tissue pathological levels. Accordingly, spatially resolved spectroscopy provides an oppor-

tunity to separate layered-specific tissue absorption from the bulk measurement. Thus, for the superficially probing fiber geometry, it is desirable to have minimal perturbations in reflectance spectra due to hemoglobin absorption, while the deeply probing geometries are needed to increase the reflectance sensitivity to hemoglobin absorption in tissue.

Similar to the scattering scenarios, three absorption scenarios are implemented in the simulation model. This model takes into account isolated absorption variations of either the superficial or basal layer, as well as simultaneous changes of tissue absorption in both layers. Here, we use the absorption coefficients of the normal and abnormal cervical epithelial tissue as the boundary values [Fig. 1(b)].[3,34] Similar to the scattering scenarios, four intermediate points are selected as the transition states of tissue dysplasia. To emphasize the effect of tissue absorption, we use the scattering coefficients of the normal epithelial tissue as a constant parameter in the model.

2.3 Fiber Geometries

Before starting the Monte Carlo simulation, solid fiber optics were computationally implemented in the simulation program to imitate realistic spatial configurations of fibers in a fiber probe. To execute this, a single illumination fiber, 100 μm in diameter, is situated at the center of the tissue model, surrounded by a ring of 12 collection fibers, also 100 μm in diameter and 300 μm apart, as measured center-to-center from the source fiber. The collection fibers are evenly spaced and positioned concentrically about the illumination axis; each fiber is individually modeled as a solid 3-D object. The illumination fiber is invariantly oriented flush to the surface of the tissue model, and only the angular orientation of the collection fibers is investigated. Three collection angles, 0, 40, and −20 deg, are implemented in this study. The negative angle denotes fiber rotation away from the illumination fiber. Differences in refractive indices and losses due to refraction are taken into account by the simulation program, based on the theoretical calculation of Fresnel's refraction formula. The refractive indices of the fibers and tissue in our model are 1.5 and 1.37, respectively. The nominal numerical aperture of the fibers is 0.22, modeling after common multimode fiber optics, which translates to an effective numerical aperture of 0.16 inside the tissue model.

2.4 Ray Tracing and TracePro Simulation

TracePro by Lambda Research (Littleton, Massachusetts) is the ray-tracing program used for the theoretical calculation of photon propagation in the tissue model. TracePro utilizes the well-established Monte Carlo solid modeling method to simulate photon interactions with tissue. The human interface of TracePro is similar to that of CAD, which allows users to create necessary geometric details of the model. Particulars about Monte Carlo modeling can be found in many published scientific texts.[48–53]

In TracePro, illumination photons are guided through a perpendicularly oriented source fiber at the center of the tissue surface via an effective numerical aperture of 0.16, as noted before. An evaluation of simulation convergence had already been conducted prior to the initiation of this study. At that time, we ran ten groups of provisional simulations with in-

creasing numbers of incident rays, and calculated the detected reflectance convergence. With a ray count of 10 million per wavelength, the maximum standard error among the ten trial simulations across the entire spectrum was no greater than 5%. Therefore, we determined that 10 million incident photons were sufficient to provide necessary simulation convergence. 40 million photons per wavelength are used in the final simulations to have extra data sampling. MATLAB version 7.0 by Mathworks, Incorporated (Natick, MA) is used for postsimulation data processing.

In this spectral simulation study, we are primarily interested in the reflectance spectra sampled under different tissue optical properties using the fiber geometries indicated earlier. Detected photons (simulated separately for each wavelength) and their remnant photonic weights (1 being the initial value) are summed to give the total detected reflectance at each simulated wavelength. The penetration depth (Z_{max}) of a single photon is defined as the greatest axial displacement of photon propagation. Although Z_{max} does not completely represent the spatial distribution of photons in tissue, since it only quantifies photon propagation in the axial direction, it is an appropriately indicative metric for the characterization of photon penetration in tissue and can be directly correlated to actual tissue depths. As the spatial metric, characterizing individual photons, is properly defined, its weighted average with respect to individual photons' contribution to the overall reflectance is taken. This is done to give a proper valuation of the probing capability of the fiber probes as a whole. Let the weight of each detected photon be f, the number of detected photons NP, and the total reflectance R. Then the expected value of probing depth at that wavelength is formulated as the following:

$$Z(\lambda)^{\text{probe}} = \frac{\sum_{j=1}^{NP} f_j(\lambda) \cdot Z(\lambda)_{\text{max}_j}}{\sum_{j=1}^{NP} f_j(\lambda)} = \frac{\sum_{j=1}^{NP} f_j(\lambda) \cdot Z(\lambda)_{\text{max}j}}{R(\lambda)}. \quad (1)$$

3 Results

3.1 Changes in Scattering Coefficients

Figures 2(a)–2(c) show the reflectance detected by the 0-deg collection fibers at 300-μm SDSD when the scattering coefficients are varied in the epithelial, stromal, and both layers, respectively. The fluence values are referenced to the peak of the normal tissue's spectra, so that the differences among the simulated reflectance spectra can be easily assessed. As the epithelial scattering increases nearly threefold from the normal to abnormal state, we expect to detect more early returning photons reemitted from the superficial layer. However, and contrary to our expectations, a slight downward trend in the detected reflectance is observed for the 0-deg collection fibers. Based on diminishing fluence levels, together with the opposing phenomenon of increasing superficial scattering, we conclude that the 0-deg fiber geometry may be predominantly sensitive to the basal stromal layer.

Figures 3(a)–3(c) depict the detected reflectance by the 40-deg collection fibers, and the optical properties of the tis-
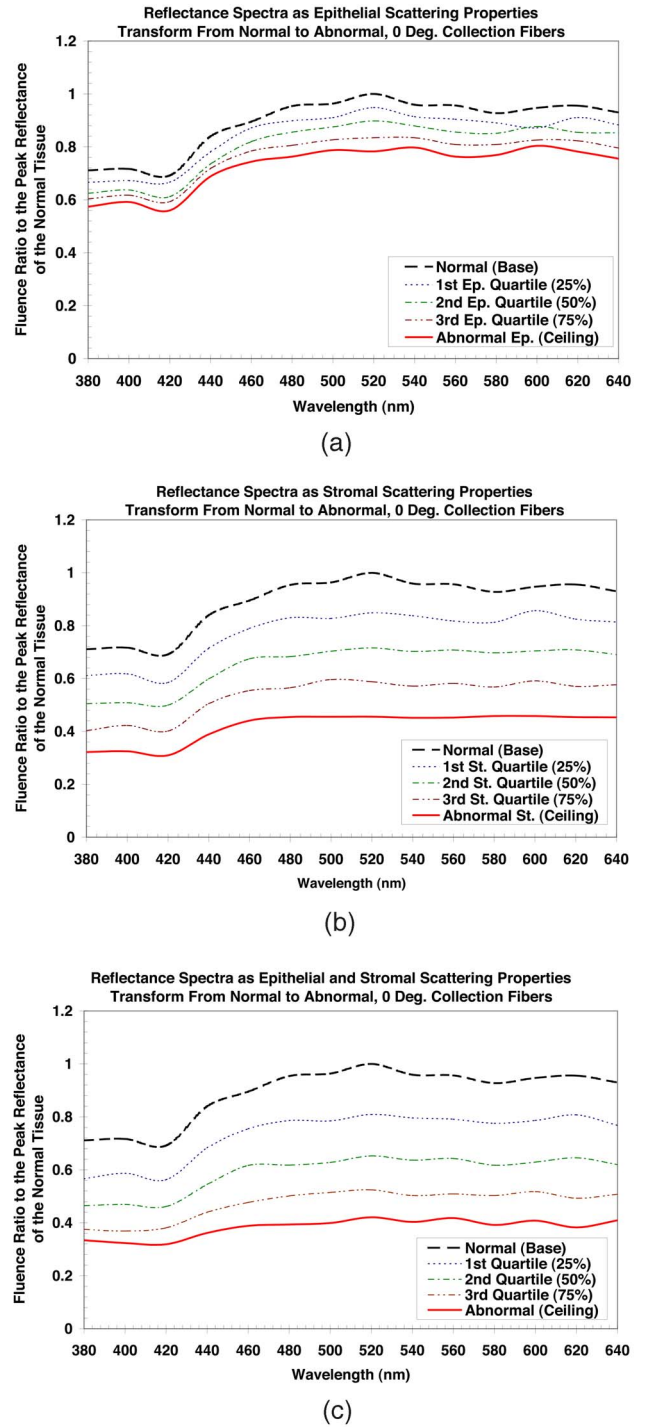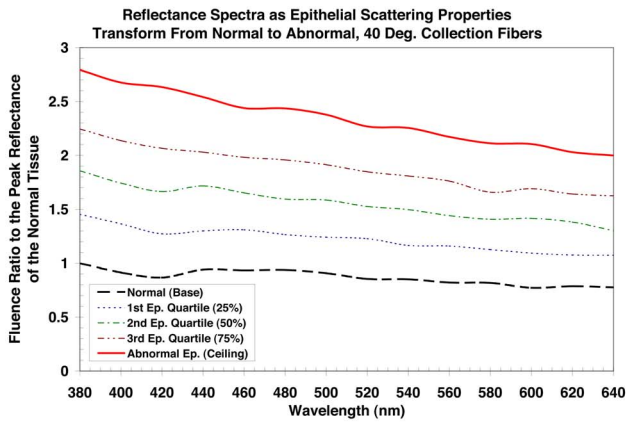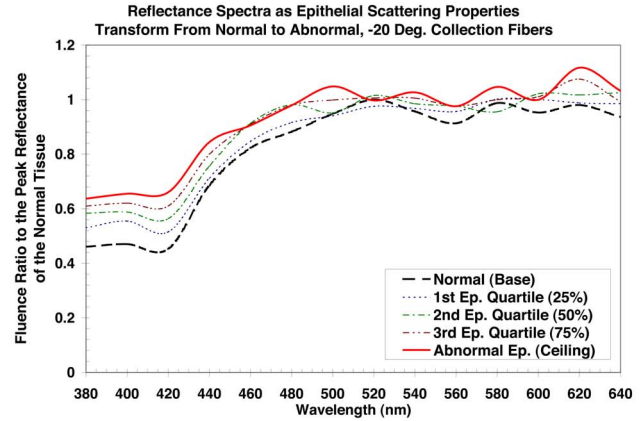

(a)

(b)

(c)

Fig. 2 (a), (b), and (c) Reflectance spectra detected by the 0-deg collection fibers when tissue scattering coefficients progress from the normal to abnormal conditions in the epithelial, stromal, and both layers, respectively; the values of fluence are referenced to the peak of the normal tissue.
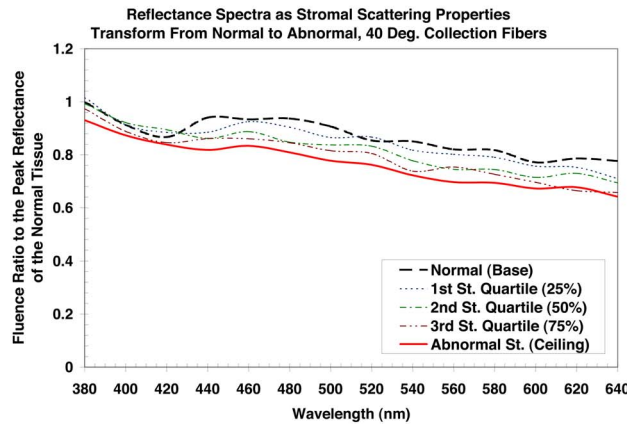
sue model are identical to those implemented previously. Contrary to the orthogonal fibers, this obliquely oriented fiber geometry accurately probes the epithelial layer, which is its expected target, and yields reflectance spectra consistent with the rising trend of the epithelial scattering, as epithelial dys-
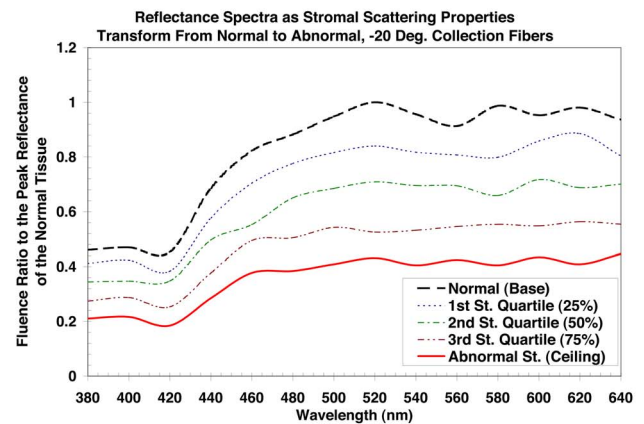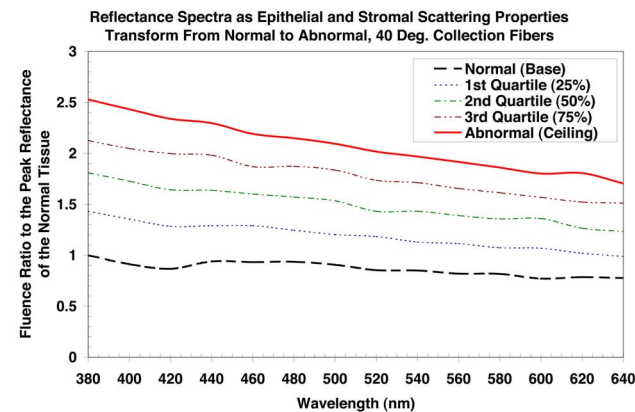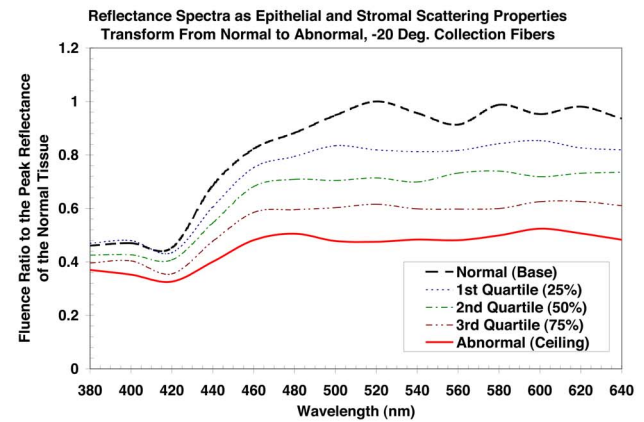
(a)

(b)

(c)

Fig. 3 (a), (b), and (c) Reflectance spectra detected by the 40-deg collection fibers when tissue scattering coefficients progress from the normal to abnormal conditions in the epithelial, stromal, and both layers, respectively; the values of reflectance fluence are referenced to the peak of the normal tissue.

(a)

(b)

(c)

Fig. 4 (a), (b), and (c) Reflectance spectra detected by the −20-deg collection fibers when tissue scattering coefficients progress from the normal to abnormal conditions in the epithelial, stromal, and both layers, respectively; the values of reflectance fluence are referenced to the peak of the normal tissue.

plasia progresses. Additionally, the fluence levels and spectral structures of the reflectance curves shown in Figs. 3(a) and 3(c) are in general agreement. This indicates that the stromal variations additionally included in Fig. 3(c) do not significantly alter the results. At the same time, Fig. 3(b) corroborates this conclusion by demonstrating that variations in the

stromal scattering only produce limited changes in the reflectance spectra, which are sampled with the 40-deg collection fibers.

In Figs. 4(a)–4(c), where the reflectance spectra yielded by

Table 1 Area under curve with respect to various combinations of tissue scattering properties and fiber geometry; values are normalized to the dataset of the normal tissue. Greater deviations from the normal tissue indicate strong fiber probing sensitivity and correlation to corresponding tissue layers.

Collection fiber angle	Layer under Investigation	Tissue scattering transition				
		Normal	25%	50%	75%	100% (Abnormal)
0 deg	Epithelium	1	0.95	0.90	0.86	0.82
	Stroma		0.86	0.73	0.60	0.47
	Both		0.83	0.66	0.53	0.43
40 deg	Epithelium	1	1.40	1.79	2.15	2.68
	Stroma		0.97	0.94	0.91	0.88
	Both		1.36	1.71	2.05	2.38
−20 deg	Epithelium	1	1.03	1.06	1.09	1.12
	Stroma		0.86	0.71	0.57	0.43
	Both		0.88	0.77	0.66	0.54

the −20-deg fibers are shown, we can see that the changes in epithelial scattering only produce limited perturbations on the spectra, whereas much more pronounced differences in the spectral fluence and structure are seen for the cases involving changes in stromal scattering properties.

Quantitatively, Table 1 tabulates the "area under curve" (AUC) values of the spectra with various combinations of fiber angles and tissue scattering properties. The dataset of the normal tissue is designated as the reference and normalized to one. For fiber geometry insensitive to changes in the scattering property of a particular tissue layer, AUC should remain relatively unperturbed, while acute changes in AUC typically indicate a strong sensitivity to the particular layer under investigation. Neither the 0- nor −20-deg fibers yield significant differences in AUC when the epithelial layer is the sole subject of investigation. The 40-deg fibers are particularly insensitive to the changes in stromal scattering, while significant changes in AUC are seen for the same fiber geometry as the epithelial model transforms from normal to abnormal. This strong correlation with the epithelial layer suggests that the 40-deg fibers have the potential to detect tissue pathology inside epithelia at an earlier time than the 0- and −20-deg fibers.

In addition to the spectral relationship between the fiber geometry and tissue scattering, the probing depths of a fiber probe may also be affected by the changes in a tissue's optical properties. Our simulation results show that the probing depths of all three fiber probes gradually increase with increasing wavelengths. This occurs because tissue is generally less scattering and absorptive at longer wavelengths. The trend of increasing probing depths with respect to longer

wavelengths is consistent. Thus, for brevity, only two representative wavelengths (420 and 580 nm, representing the wavelengths on the shorter and longer ends of the spectrum, respectively) are shown. The selective wavelengths are indeed representative of the entire spectrum as regarding the penetration depths in tissue with respect to different fiber geometries. Table 2 tabulates the expected probing depths, as defined in Eq. (1), with respect to the combinations of fiber geometries and tissue scattering conditions discussed thus far, at wavelengths of 420 and 580 nm, respectively. In the parentheses following the expected probing depths, we include the standard deviations with respect to the computed means by Eq. (1). Mathematically, the standard deviations are a measure of distribution variation with respect to the mean values. In the context of this study, the standard deviations denote the spatial selectivity of the fiber probes. It must be noted that the standard deviations here should not be regarded as the level of convergence of the Monte Carlo simulations; instead, they should be viewed as the ranges of probing depths extended bilaterally from the expected probing depths.

3.2 Changes in Absorption Coefficients

Although the tissue absorptions of both the epithelial and stromal layers are investigated, only the stromal absorption is presented here. Our simulations indicate that epithelial absorption coefficients only impose minuscule perturbations to the overall spectra. Using the metric AUC, we determine that the greatest difference in overall reflectance fluence among the simulated epithelial-only models is approximately 1%; thus, we are unable to make definitive discriminations among the spectra, since all spectra virtually overlap for all three configurations of fiber geometry. Since the thickness of the epithelial layer is small, the path lengths traversed by photons in the epithelial layer are most likely too small to create significant changes due to epithelial absorption. In addition, since the levels of variation in epithelial absorption associated with tissue pathology are considerably smaller in magnitude than those involving stromal absorption, we do not include epithelial absorption here.

Figures 5(a)–5(c) show the reflectance spectra of the 0-, 40-, and −20-deg collection fibers, respectively; both the epithelial and stromal absorption coefficients sequentially transit from the normal to abnormal state. Comparing the spectra among the three subfigures, we see that the presence of hemoglobin absorption is the least evident in the spectra collected by the 40-deg fibers and the most evident for the −20-deg. fibers, as gauged by the reflectance fluence at the Soret (420 nm) and Q-band (540 and 580 nm) wavelengths. To quantify the sensitivity of the fibers to tissue absorption, we use the metric AUC to measure the change in overall reflectance with respect to varying tissue absorption, and these data are shown in Table 3. Based on the numerical results shown in Table 3, it is clear that epithelial absorption properties have only very limited influence on the overall fluence levels of detected reflectance, while comparatively, stromal absorption is the main source of reflectance attenuation. Figure 6 specifically demonstrates the trend of decreasing AUC, as tissue absorption in both layers increases from normal to abnormal levels in tandem. The results suggest that the
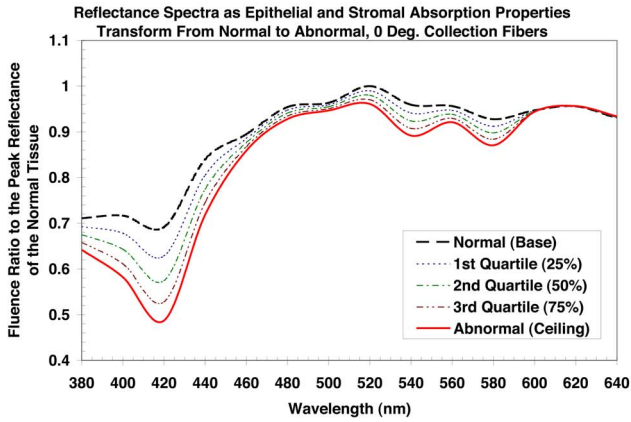
Table 2 Mean and standard deviation of fiber probing depths with respect to various combinations of tissue scattering properties and fiber geometry; values are shown in the unit of μm. The standard deviations enclosed in the parentheses represent the range of fiber probing depths extended bilaterally from the means.

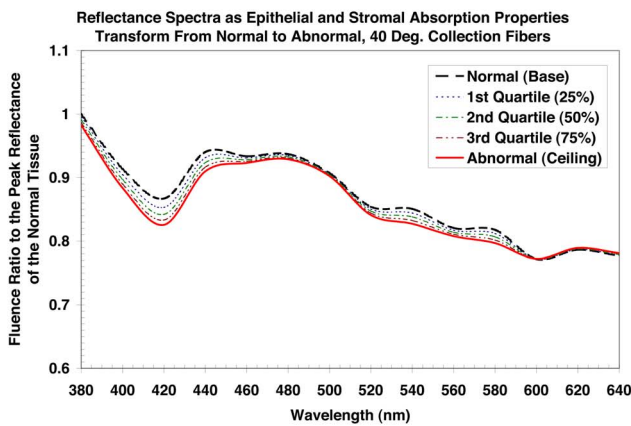| Collection fiber angle	Layer under investigation	Tissue scattering transition at 420 nm				
		Normal	25%	50%	75%	100% (Abnormal)
0 deg	Epithelium	600(85)	585(90)	573(95)	551(103)	534(112)
	Stroma		603(85)	611(91)	619(96)	624(102)
	Both		591(91)	570(103)	541(124)	500(147)
40 deg	Epithelium	136(88)	122(61)	116(50)	115(48)	113(48)
	Stroma		126(66)	119(48)	116(46)	114(42)
	Both		117(49)	112(45)	109(43)	106(42)
−20 deg	Epithelium	673(118)	644(111)	621(116)	589(122)	557(129)
	Stroma		683(123)	685(127)	698(147)	717(161)
	Both		654(123)	624(135)	586(159)	541(168)
Collection fiber angle	Layer under investigation	Tissue scattering transition at 580 nm				
		Normal	25%	50%	75%	100% (Abnormal)
0 deg	Epithelium	694(145)	681(144)	670(145)	656(144)	644(144)
	Stroma		702(152)	719(163)	741(177)	751(191)
	Both		689(152)	682(158)	675(181)	647(206)
40 deg	Epithelium	221(213)	175(154)	157(124)	141(97)	127(75)
	Stroma		204(200)	177(163)	159(133)	135(76)
	Both		169(144)	133(76)	122(52)	115(46)
−20 deg	Epithelium	853(210)	825(210)	797(214)	778(207)	759(200)
	Stroma		878(225)	899(246)	939(257)	994(307)
	Both		843(217)	834(232)	815(262)	804(284)

−20-deg fibers, by virtue of their deep probing depths, are more responsive to the changes in stromal absorption by showing 11 percentage points of variation in AUC. On the other hand, the 40-deg fibers only have about 2 percentage points of variation in the AUC metric.

Table 4 shows another method of quantifying the fibers' probing sensitivity to the stromal layer. This method measures the levels of reflectance depression at hemoglobin's Soret wavelength (420 nm) with respect to various combinations of tissue absorption properties and fiber geometries. Using the normal 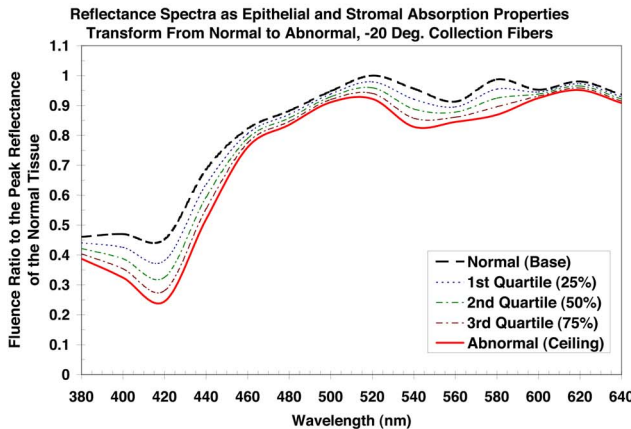tissue model as the reference, we are able to assess the rate of reflectance attenuation at the Soret wavelength correlated to the transition of tissue absorption from the normal to abnormal states. This metric is particularly pertinent to the interpretation of hemoglobin absorption in the reflectance spectra: as hemoglobin concentration increases with angiogenesis in diseased tissue, further depressed reflectance fluence is seen with the 0- and −20-deg fibers, whereas only limited deviations are observable for the 40-deg fibers, which further confirm their insensitivity to hemoglobin interference using the 40-deg fiber geometry.

(a)

(b)

(c)

Fig. 5 (a), (b), and (c) Reflectance spectra detected by the 0-, 40-, and −20-deg collection fibers, respectively, when tissue absorption coefficients progress from the normal to abnormal conditions in both layers; the values of reflectance fluence are referenced to the peak of the normal tissue.

Table 3 Area under curve with respect to various combinations of tissue absorption properties and fiber geometry; values are normalized to the dataset of the normal tissue. Greater deviations from the normal tissue indicate strong fiber probing sensitivity and correlation to corresponding tissue layers.

Collection fiber angle	Layer under investigation	Tissue absorption transition					
		Normal	10%	25%	50%	75%	100% (Abnormal)
0 deg	Epithelium	1	1.00	1.00	1.00	1.00	1.01
	Stroma		0.99	0.98	0.96	0.94	0.93
	Both		0.99	0.98	0.97	0.95	0.93
40 deg	Epithelium	1	1.00	1.00	1.00	1.00	1.00
	Stroma		1.00	0.99	0.99	0.98	0.98
	Both		1.00	0.99	0.99	0.99	0.98
−20 deg	Epithelium	1	1.00	1.00	1.00	1.01	1.01
	Stroma		0.99	0.97	0.94	0.91	0.88
	Both		0.99	0.97	0.94	0.91	0.89

ferent fiber geometries are used. From the results collectively shown in Sec. 3.1, it is clear that changes in epithelial scattering coefficients are best detected by the 40-deg collection fibers, which produce the most discernable contrast among the simulated reflectance spectra, as the epithelial scattering coefficients increase from normal (low) to abnormal (high) levels [Fig. 3(a)]. At the same time, the 40-deg fibers are insensitive to changes in the stromal layer by yielding nearly identical reflectance spectra, regardless of the stromal scattering conditions [Fig. 3(b)]. In addition, the increase in epithelial scattering coefficients is accurately manifested in the reflectance spectra with the 40-deg fibers. More specifically, the fluence levels of the spectra consistently increase as the epithelial
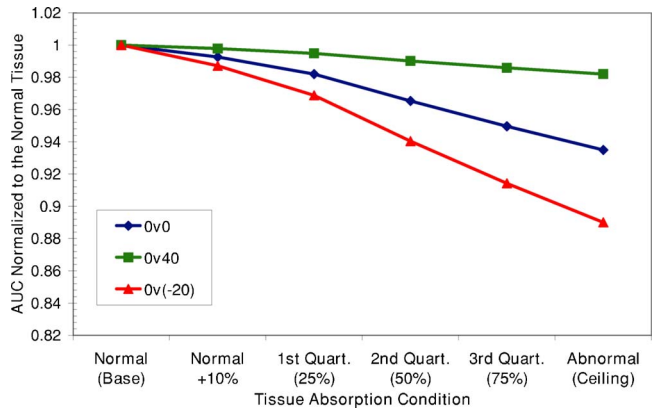

Fig. 6 Normalized areas under curve calculated for the 0-, 40-, and −20-deg collection fibers, respectively, when tissue absorption coefficients progress from the normal to abnormal conditions in both layers; the values of AUC are referenced to those of the normal tissue.

4 Discussion

4.1 *Sensitivities to Changes in Layer Scattering*

In this study, we investigate the sensitivity of reflectance spectroscopy to changes in tissue scattering properties when dif-

Table 4 Level of reflectance fluence at hemoglobin's Soret wavelength (420 nm) with respect to various combinations of tissue absorption properties and fiber geometry; values are normalized to the dataset of the normal tissue. Greater deviations from the normal tissue indicate strong fiber probing sensitivity to hemoglobin presence.

Collection fiber angle	Layer under investigation	Tissue absorption transition					
		Normal	10%	25%	50%	75%	100% (Abnormal)
0 deg	Epithelium	1	1.00	0.99	0.98	0.97	0.97
	Stroma		0.96	0.92	0.84	0.78	0.73
	Both		0.96	0.91	0.83	0.76	0.70
40 deg	Epithelium	1	1.00	0.99	0.99	0.98	0.98
	Stroma		0.99	0.99	0.98	0.97	0.97
	Both		0.99	0.98	0.97	0.96	0.95
−20 deg	Epithelium	1	1.00	0.99	0.98	0.97	0.96
	Stroma		0.94	0.86	0.74	0.65	0.58
	Both		0.94	0.85	0.73	0.63	0.56

layer transforms from normal to abnormal. This is expected because, as the epithelial scattering coefficients increase nearly threefold, more photons should reemit from the superficial layer and increase the reflectance fluence. However, decreasing trends in the simulated reflectance are observed for the 0-deg collection fibers [Fig. 2(a)]. Diminishing fluence levels, together with the opposing phenomenon of increasing superficial scattering, indicate that this fiber geometry may be predominantly sensitive to the basal stromal layer. This is true because, with greater superficial scattering, it is likely that more photons are scattered and reemitted in shallow depths that are not detectable by the 0 collection fibers. Although the source-detector separation distance (SDSD) is quite small (300 μm), the majority of early returning photons remains near the source fiber, which is outside the detection space of the collection fibers. Consequently, the increase in the superficially scattered rays does not contribute to the overall reflectance. By the same argument, the rise in superficial scattering should reduce the number of photons that reach the basal layer, where the 0-deg fibers gather the majority of reflectance signals. As a result, reductions in reflectance fluence are seen here. The suggestion that the 0-deg fibers are deeply probing is supported by the comparisons between Figs. 2(b) and 2(c). Specifically, as tissue transforms from the normal to diseased states, the scattering coefficients of the basal stromal layer also decrease. Under these conditions, the detected reflectance correspondingly diminishes with the downward trend of stromal scattering. Furthermore, the reflectance spectra shown in Figs. 2(b) and 2(c) are similar in both magnitude and structure, which suggests the limited influence of epithelial scattering in the resultant spectra.

Similar to the 0-deg fibers, the resultant reflectance spectra simulated with the −20-deg fibers also demonstrate limited sensitivities to the changes in epithelial scattering properties.

The negative prefix of the −20-deg fibers denotes an opposite rotation about the source fiber such that the angled fibers have their distal facets facing away from the illumination point. By blocking the intake of superficially scattered photons, this particular fiber geometry probes deeper into the tissue and, consequently, yields spectra that are more responsive to the changes in stromal tissue properties.

4.2 Disparities between the 0 and −20–Deg Fibers

Although both the 0 and −20-deg fibers are expected to probe deeply into the tissue, we observe an interesting disparity in their reflectance spectra, as shown in Fig. 2(a) for the 0-deg fibers and Fig. 4(a) for the −20-deg fibers. In Fig. 2(a), the fluence level decreases with increasing epithelial scattering coefficients. This may be attributed to both the loss of superficially scattered photons that are not detectable by the collection fibers, and consequent reduction in photons entering the stromal layer, as discussed previously. However, this effect does not seem to apply to the −20-deg fibers, which, in contrast, exhibit a gain in reflectance fluence as a result of increasing epithelial scattering. To further explain the apparent disparity between these two similarly deeply probing fiber geometries, we analyze the spatial distributions of the collected photons to gather more information about the photon collections of both fiber geometries. Beginning with the simplest representation of photon distributions in tissue, Fig. 7 demonstrates the depth-wise distribution of reflectance detected by the 0- and −20-deg fibers under low (μs =4.82 mm^{-1}) and high (μs=14.2 mm^{-1}) epithelial scattering coefficients that respectively represent the normal and abnormal epithelial scattering properties implemented in the tissue model. The horizontal axis is partitioned every 10 μm, and the peak fluence is normalized to 1 to enable easy compari-
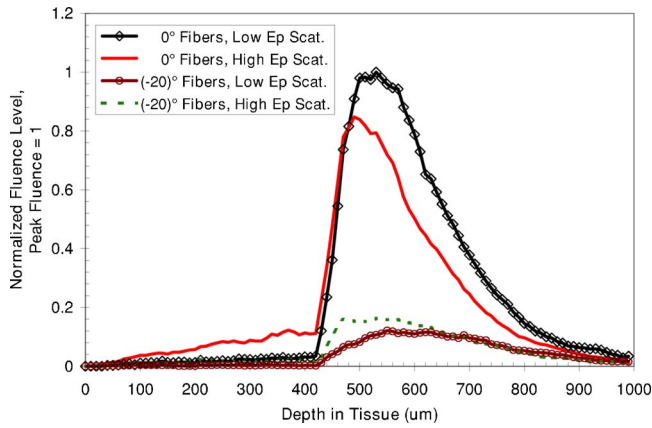
Fig. 7 Depth-wise distribution of reflectance detected by the 0- and −20-deg collection fibers under low (μs=4.82 mm^{-1}) and high (μs =14.2 mm^{-1}) epithelial scattering conditions that respectively represent the normal and abnormal epithelial scattering properties implemented in our tissue models. The horizontal axis is partitioned into sections of 10 μm, and the peak fluence is normalized to one.

Fig. 8 The lateral density distribution of detected reflectance, as measured from the center of the source fiber, as photons reach their respective maximum probing depths in tissue. Both instances of the 0- and −20-deg collection fibers under low (μs=4.82 mm^{-1}) and high (μs=14.2 mm^{-1}) epithelial scattering conditions, which respectively represent the normal and abnormal epithelial scattering properties, are demonstrated. The horizontal axis is partitioned into sections of 10 μm.

sons among the curves. These reflectance data are sampled at the 380-nm wavelength and verified to be representative of the general trends across the spectrum. The common responses to increasing epithelial scattering between the 0- and −20-deg fibers are the moderate rises in superficial reflectance from the epithelial layer, seen before the 450-μm mark on the abscissa, and leftward shifts of peak stromal reflectance to the epithelium-stroma interface. This explains the decrease in tissue probing depths, as the superficial layer becomes more scattering. However, the 0-deg fibers have a significant decline in stromal reflectance under the higher epithelial scattering condition, which, in effect, lowers the overall reflectance, despite the moderate increase in superficially scattered signal. Interestingly, the −20-deg fibers do not suffer the same loss in reflectance fluence as the 0-deg fibers. Instead, there is a gain of reflectance distributed in both epithelial and stromal layers for the −20-deg fibers with greater epithelial scattering.

The causes of the variations in the depth-resolved reflectance may be better understood when the lateral distributions of detected reflectance are analyzed. To illustrate this, Fig. 8 shows the density distribution of the collected photons with respect to the lateral distances measured from the illumination point when the photons reach their respective maximum probing depths in tissue. The −20-deg fibers, by virtue of their outwardly rotated facets, are able to detect photons farther away from the source fiber, as opposed to the 0-deg fibers, which primarily gather photons in the tissue volume between the source and collection fibers. The extended detection range of the −20-deg fibers may enable greater collection of the photons scattered in the stromal layer and thereby create a gain in the overall reflectance fluence.

Although Figs. 7 and 8 may reveal some important insights into the changes of reflectance distribution where tissue scattering is concerned, the information is, nonetheless, one dimensional. For better qualitative understanding of photon distribution in the tissue models, the maps of fluence distribution are used to provide simultaneous information about optical fluence and spatial distribution in both axial and radial directions, as shown in Figs. 9(a)–9(d). In these figures, the ab-
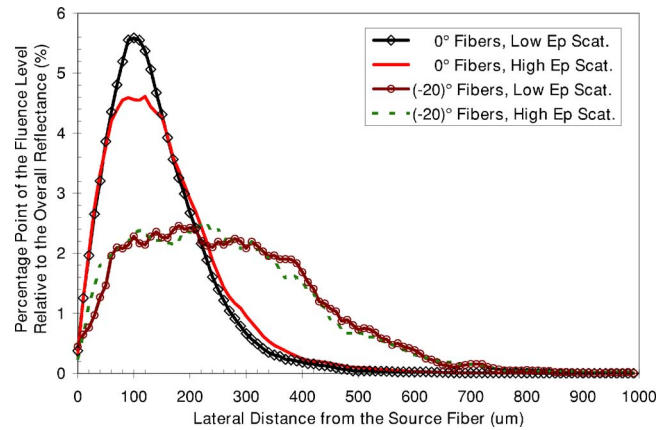
scissa denotes the lateral positions of the moving photons in tissue, and the ordinate denotes the axial positions measured from the tissue surface. It should be noted that only the collected photons are shown in the maps; hence, the data provided in these figures do not account for photons that are lost or rejected by the collection fibers. For the 0-deg fibers [Figs. 9(a) and 9(b)], with greater epithelial scattering, the injected photons diverge quickly and lift the overall distribution toward the tissue surface. However, the fluence level near the epithelium-stroma interface has become less concentrated and thus results in a loss of detected reflectance from the same region. Similar observations can be made for the −20-deg fibers, with the exception that appreciable gains in both epithelial and total reflectance are observed where there is stronger epithelial scattering. When the tissue model employs the greater epithelial scattering coefficients, the −20-deg fibers detect more photons near the epithelium-stroma interface [Fig. 9(d)], whereas the lesser scattering epithelial layer leads to a less efficient reflectance gathering from the same region of the tissue [Fig. 9(c)]. To explain this phenomenon, we believe that the stronger epithelial scattering causes the incident photons to diverge more quickly and that this then results in a rise in reflectance carried by photons near the epithelium-stroma boundary. The radius of incident beam, expanded by the stronger epithelial scattering, seems to escape the effective detection region of the 0-deg collection fibers; consequently, we observe a decrease in detected fluence inside the stromal layer that overshadows the moderate gain in epithelial reflectance, and consequently results in a net loss in the overall reflectance. On the other hand, the expanded incident beam better illuminates the tissue space visible to the outwardly rotated −20-deg fibers, which consequently results in greater reflectance sampled from the tissue.

4.3 Assessment of Probing Depths

In addition to the spectral relationship between the fiber geometry and tissue scattering, the probing depths of a fiber
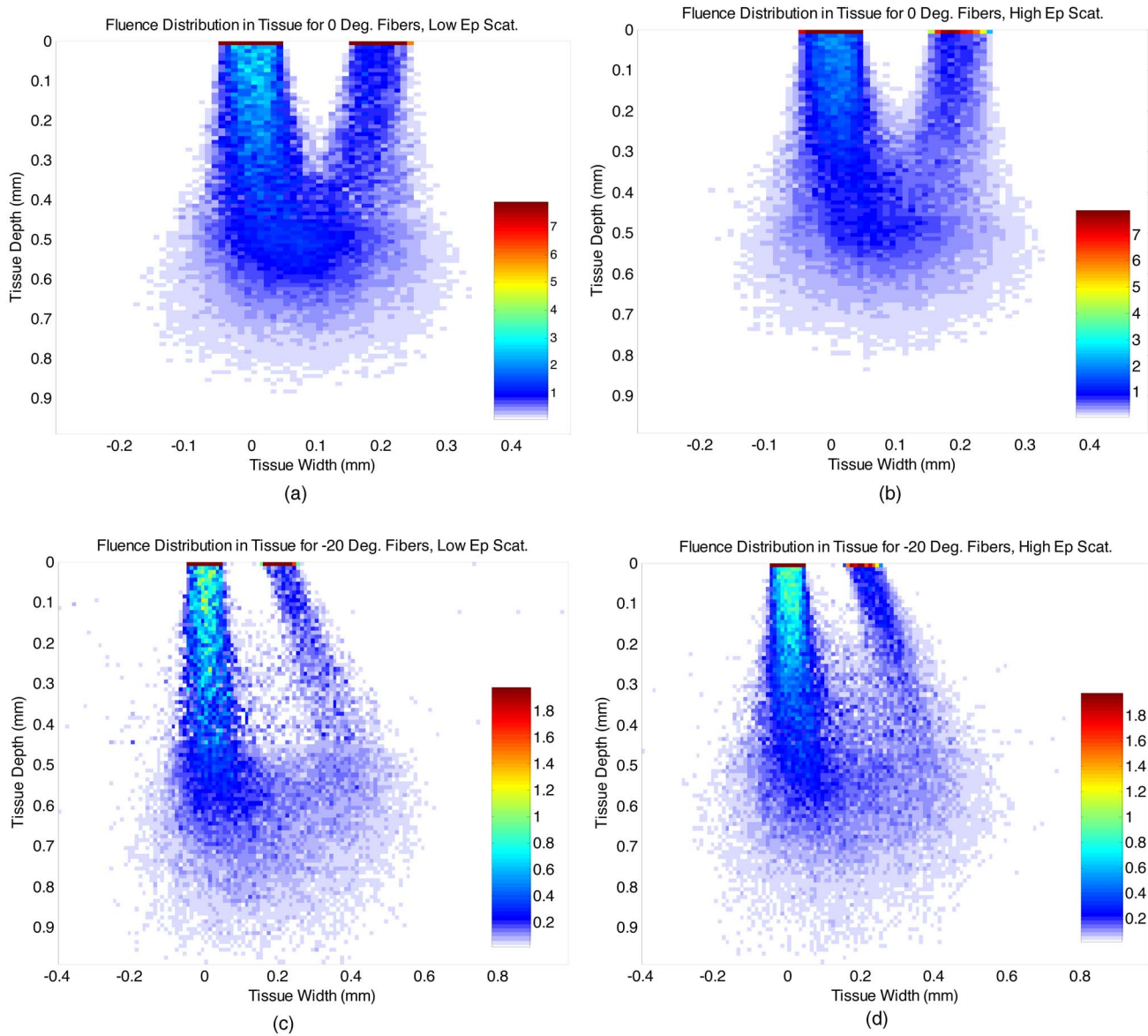
Fig. 9 (a) through (d) Internal fluence distribution in tissue for 0- and −20-deg fibers under low ($\mu s=4.82$ mm^{-1}) and high ($\mu s=14.2$ mm^{-1}) epithelial scattering conditions that respectively represent the normal and abnormal epithelial scattering properties implemented in our tissue models. The grid size is 10×10 μm.

probe may also be affected by the changes in tissue scattering properties. For the 0-deg fibers, the increasing epithelial scattering shifts the proportionality of detected reflectance toward the surface and results in a trend of decreasing probing depths. However, a less intuitive result is that the reduction in the stromal scattering also increases the probing depths when the epithelial scattering remains constant. Conventionally, reduction in stromal scattering should decrease the amount of photons reemitted from the basal layer and shift the spatial emphasis to the superficial layer. In fact, while that may be true for some cases, our simulation data indicate that smaller stromal scattering coefficients allow photons to penetrate more deeply and travel greater distances in the tissue model before detection by the collection fibers. This prolonged tissue penetration may well offset the reduction of stromal reflectance in the calculation of probing depths [Eq. (1)], and an

increase in the calculated probing depths is therefore seen as associated with decreasing stromal scattering. Once the scattering transitions in both layers are combined, the probing depths are further reduced as tissue scattering conditions transform from normal to abnormal. The combination of high epithelial and low stromal scattering coefficients strongly diminishes the number of reflected rays from the basal layer and, consequently, further amplifies the reduction in probing depths, in spite of the prolonged penetration depths and path lengths of individual photons in the stromal layer.

Compared to the 0-deg fibers, the probing depths of the 40-deg fibers show a different dependence on the scattering properties of the tissue model, as the probing depths decrease in all three scenarios of tissue scattering. It should be recalled that moderately deeper depths are achieved with decreasingly intensive stromal scattering when the 0-deg fibers are used;

however, in the instance of the 40-deg fibers, the probing depths are shifted toward the tissue surface under the same scattering conditions. According to the numerical results of our simulation, there is a significant reduction in the number of photons that penetrate to the region near the epithelium-stroma interface. In other words, there is a loss of reflectance that originates from the basal epithelium and top of the stroma. The exclusion of these moderately penetrating photons shifts the weight of reflectance distribution toward the surface. This loss can be elucidated by the scattering coefficients of the stroma, which acts as a background reflector underneath the epithelial layer. As the scattering coefficients of the stromal layer decrease, more photons are able to propagate into the deeper space of the tissue model and then exit outside the collecting region of the 40-deg fibers. These photons, however, are better sampled by the 0- or −20-deg collection geometry, as both result in a deeper distribution of detected reflectance. The probing depths of the −20-deg fibers trend in the same way as those of the orthogonal fibers, and are therefore not repeated here.

4.4 *Sensitivities to Changes in Absorption*

Based on the spectra shown in Fig. 5, it is evident that hemoglobin, being the dominant chromophore in tissue, strongly affects the fluence levels and shapes of the reflectance spectra. In Fig. 5, the presence of hemoglobin absorption is the least evident in the spectra collected by the 40-deg fibers and the most evident for the −20-deg fibers, as gauged by the reflectance fluence at the Soret (420 nm) and Q-band (540 and 580 nm) wavelengths. As tissue absorption coefficients increase with increased tissue abnormality, the reflectance levels for all three fiber geometries correspondingly decrease. However, our data, as shown in Table 3, indicate that the 40-deg fibers are minimally affected by the changes in stromal absorption coefficients due to their highly selective probing sensitivity to the epithelial layer. On the other hand, the −20-deg fibers yield reflectance spectra for which the fluence levels are strongly sensitive to the increase in stromal absorption. These results indicate that the −20-deg fibers may be better utilized to target neovascularization in the stromal region, whereas the 40-deg fibers can better eliminate hemoglobin interference when only superficial epithelium is the target of interest.

5 Conclusion

Based on our computational results, we demonstrate that an increase in fiber obliquity with respect to the target surface yields greater sensitivity to the superficial region of the target.[27–29] Nevertheless, the spatial selectivity of fiber geometry also directly depends on the scattering and absorption properties of targeted regions in a turbid medium. Adopting a two-layer stratified epithelial tissue model, this study specifically assesses the effects of tissue scattering and absorption to the spatial selection of reflectance sampling using angularly variable fiber geometry.

Three angular configurations, 0-, 40-, and −20-deg collection fibers, are placed in contact with the tissue model, and reflectance spectra are computed using Monte Carlo simulation. The 0-deg collection fibers, placed at SDSD of 300 μm, are primarily affected by the changes of optical properties in the stromal layer of the tissue model. Decreasing scattering

coefficients of the stromal layer significantly reduce the level of reflectance collected at the tissue surface. More sensitive assessments of the stromal layer, however, can be made when the −20-deg collection fibers are used in place of the orthogonal fibers. On the other hand, when the epithelial layer is the sole variable in the model, neither the 0- nor −20-deg fiber geometry yields significant changes in their respective reflectance spectra. In addition, the shifts in spectral fluence and structures for both the 0- and −20-deg fibers are much more subdued, whereas the 40-deg fibers are particularly sensitive to the values of epithelial scattering. The AUC metric indicates a 250% gain in reflectance fluence as the epithelial scattering condition transforms from normal (low) to abnormal (high). This acutely rapid response to epithelial scattering is a promising indication that the 40-deg fibers may more sensitively probe the physiological conditions of the epithelial layer.

From the perspective of tissue absorption, we are interested in the effect of stromal absorption, largely due to hemoglobin, on the performance of the fibers. Epithelial absorption does not vary significantly enough to produce appreciable distinctions among the reflectance spectra for all fibers. We believe that, because the thickness of epithelium is typically within a few hundred micrometers, the epithelial layer does not provide the path lengths necessary for significant attenuation in photonic weights. The simulation results confirm our hypothesis by showing only miniscule distinctions among reflectance spectra when epithelial absorption coefficients are the only variable in the model. Conversely, stromal absorption dominantly affects the spectral fluence and structure of detected reflectance. The deeply probing fiber probes, to include the 0- or −20-deg collection fibers, are particularly responsive to the levels of stromal absorption when such sensitivities are measured by the AUC. For instance, a 12% reduction in the AUC and a 44% reduction in the reflectance at the Soret wavelength (420 nm) are observed for the −20-deg fibers as the stromal absorption increases from the normal to abnormal state. Approximately 7 and 30% reductions, with respect to the AUC and Soret reflectance, are seen for the 0-deg fibers. Under the same conditions, the superficially sensitive 40-deg fibers only exhibit mere 2 and 5% decreases, correspondingly.

Achieving spatially resolved reflectance spectroscopy by the use of angularly variable fiber geometry does seem promising. However, there remain a few issues that require further investigation before such techniques can be widely applied to clinical implementation, especially those involving *in-vivo* applications. For instance, depending on the target tissues, some *in-vivo* measurements may pose a restriction on the size of fiber probes that can be properly fitted into bodily orifices. Also, to avoid permanent fractures to the fibers, the physical dimension of the probes must accommodate the added spatial requirement of direct fiber rotation and may consequently become too rigid and bulky to maneuver in some bodily orifices. If, however, alternative methods of angular variability are available, significant fiber rotation may not be necessary. For example, facet beveling, to a certain extent, bends the optical axis of fiber optics, and when combined with moderate fiber rotation, the desired collection angles can be achieved without overly expanding probe sizes. Ray-guiding optical elements have also been used in various side-viewing probes to achieve an effect similar to angled collection.[27,31]

In summary, we complete a model-based simulation study that encompasses the use of angularly variable fiber geometry to achieve spatially resolved reflectance measurements in a two-layer tissue model. Based on the results of our study, we believe that oblique fiber geometry can effectively resolve the changes in tissue properties in layered tissue structures. As shown in this study, the 40-deg fiber geometry is capable of accurately detecting the increasing scattering coefficients of the epithelial layer. The resultant reflectance spectra can be directly correlated to the scattering conditions inside the epithelium, and, at the same time, hemoglobin interference from the stroma is minimized. With the 40-deg fibers, contrast in reflectance spectra, which signifies increasing epithelial dysplasia, is much more discernable than that achieved by conventional orthogonal fibers. The enhanced sensitivity to epithelial abnormality may consequently lead to earlier disease diagnosis. We have also demonstrated that stromal tissue diagnosis can be realized using the -20-deg fibers, which are particularly sensitive to the changes in stromal tissue properties. This may be of great importance for cancer diagnosis at later stages where angiogenesis prevails in the stroma. Most importantly, this study has provided strong evidence that spatially resolved reflectance spectroscopy in tissue can be realized via this simple geometric means of varying the collection fiber angles. Finally, using this study as a foundation, our future investigations will specifically focus on angled fiber probes by using tissue phantoms, *in-vitro* tissue samples, and implementations of clinically applicable probe designs.

Acknowledgments

References

1. I. Bigio and J. R. Mourant, "Ultraviolet and visible spectroscopies for tissue diagnostics: fluorescence spectroscopy and elastic-scattering spectroscopy," *Phys. Med. Biol.* **42**, 803–814 (1997).
2. K. Sokolov, R. Drezek, K. Gossage, and R. Richards-Kortum, "Reflectance spectroscopy with polarized light: is it sensitive to cellular and nuclear morphology," *Opt. Express* **5**(13), 302–317 (1999).
3. R. Drezek, R. Richards-Kortum, M. Brewer, M. Feld, C. Pitris, A. Ferenczy, M. Faupel, and M. Follen, "Optical imaging of the cervix," 2nd Intl. Conf. Cervical Cancer, pp. 2015–2027 (2003).
4. A. Wax, J. W. Pythila, R. N. Graf, R. Nines, C. W. Boone, R. R. Dasari, M. S. Feld, V. E. Steele, and G. D. Stoner, "Prospective grading of neoplastic change in rat esophagus epithelium using angle-resolved low-coherence interferometry," *J. Biomed. Opt.* **10**(5), 051604 (2005).
5. O. A'Amar, R. Ley, and I. Bigio, "Comparison between ultraviolet-visible and near-infrared elastic scattering spectroscopy of chemically induced melanomas in an animal model," *J. Biomed. Opt.* **9**(6), 1320–1326 (2004).
6. U. Utzinger, M. Brewer, E. Silva, D. Dershenson, R. Blast, M. Follen, and R. Richards-Kortum, "Reflectance spectroscopy for *in vivo* characterization of ovarian tissue," *Lasers Surg. Med.* **28**, 56–66 (2001).
7. P. Thueler, I. Charvet, F. Bevilacqua, M. Ghislain, G. Ory, P. Marquent, P. Meda, B. Vermeulen, and C. Depeursinge, "*In vivo* endoscopic tissue diagnostics based on spectroscopic absorption, scattering, and phase function properties," *J. Biomed. Opt.* **8**(3), 495–503 (2003).
8. Y. Mirabal, S. Chang, E. Atkinson, A. Malpica, M. Follen, and R. Richards-Kortum, "Reflectance spectroscopy for *in vivo* detection of cervical precancer," *J. Biomed. Opt.* **7**(4), 587–594 (2002).
9. G. Marquez and L. Wang, "White light oblique incidence reflectometer for measuring absorption and reduced scattering spectra of tissue like turbid media," *Opt. Express* **1**, 454–460 (1997).
10. T. J. Pfefer, L. Matchette, C. Bennett, J. Gall, J. Wilke, A. Durkin, and M. Ediger, "Reflectance-based determination of optical properties in highly attenuating tissue," *J. Biomed. Opt.* **8**, 206–215 (2003).
11. N. Ramanujam, "Fluorescence spectroscopy *in vivo*," in *Encyclopedia of Analytical Chemistry*, John Wiley and Sons, Chichester, MA (2000).
12. N. Ramanujam, M. Mitchell, A. Mahadevan, S. Thomsen, A. Malpica, T. Wright, N. Atkinson, and R. Richards-Kortum, "Spectroscopic diagnosis of cervical intraepithelial neoplasia CIN *in vivo* using laser-induced spectra at multiple excitation wavelengths," *Lasers Surg. Med.* **19**, 63–74 (1996).
13. M. Canpolat and J. R. Mourant, "Particle size analysis of turbid media with a single optical fiber in contact with the medium to deliver and detect white light," *Appl. Opt.* **40**, 3792–3799 (2001).
14. M. Canpolat and J. R. Mourant, "Monitoring photosensitizer concentration by use of a fiber-optic probe with a small source-detector separation," *Appl. Opt.* **39**, 6508–6514 (2000).
15. Y. Liu, Y. L. Kim, and V. Backman, "Development of a bioengineered tissue model and its application in the investigation of the depth selectivity of polarization gating," *Appl. Opt.* **44**(12), 2288–2299 (2005).
16. A. Myakov, L. Nieman, L. Wicky, U. Utzinger, R. Richards-Kortum, and K. Sokolov, "Fiber optic probe for polarized reflectance spectroscopy *in vivo*: Design and performance," *J. Biomed. Opt.* **7**(3), 388–397 (2002).
17. J. R. Mourant, T. Fuselier, J. Boyer, T. Johnson, and I. Bigio, "Prediction and measurements of scattering and absorption overbroad wavelength range in tissue phantoms," *Appl. Opt.* **36**, 949–957 (1997).
18. S. Avrillier, E. Tinet, D. Ettori, J. Tualle, and B. Gelebart, "Influence of emission-reception geometry in laser-induced fluorescence spectra from turbid media," *Appl. Opt.* **37**, 2781–2787 (1998).
19. G. Kumar and J. Schmitt, "Optimal probe geometry for near-infrared spectroscopy of biological tissue," *Appl. Opt.* **36**, 2286–2293 (1997).
20. T. J. Pfefer, L. Matchette, and R. Drezek, "Influence of illumination collection geometry on fluorescence spectroscopy in multi-layered tissue," *Med. Biol. Eng. Comput.* **42**, 669–673 (2004).
21. T. J. Pfefer, K. Schomacker, M. Ediger, and N. Nishioka, "Multiple fiber probe design for fluorescence spectroscopy in tissue," *Appl. Opt.* **41**, 4712–4720 (2002).
22. C. Zhu, Q. Liu, and N. Ramanujam, "Effect of fiber optic probe geometry on depth-resolved fluorescence measurements from epithelial tissues: a Monte Carlo simulation," *J. Biomed. Opt.* **8**(2), 237–247 (2003).
23. T. J. Pfefer, L. Matchette, A. Ross, and M. Ediger, "Selective detection of fluorophore layers in turbid media: the role of fiber-optic probe design," *Opt. Lett.* **28**, 120–122 (2003).
24. L. Quan and N. Ramanujam, "Relationship between depth of a target in a turbid medium and fluorescence measured by a variable-aperture method," *Opt. Lett.* **27**, 102–106 (2002).
25. J. R. Mourant, J. Boyer, A. Hielscher, and I. Bigio, "Influence of the scattering phase function on light transport measurements in turbid media performed with small source-detector separations," *Opt. Lett.* **21**, 546–548 (1996).
26. T. Papaioannou, N. Preyer, Q. Fang, A. Brightwell, M. Carnohan, G. Cottone, R. Ross, L. Jones, and L. Marcu, "Effects of fiber-optic probe design and probe-to-target distance on diffuse reflectance measurements of turbid media, an experimental and computational study at 337 nm," *Appl. Opt.* **43**, 2846–2860 (2004).
27. D. Arifler, R. A. Schwarz, S. K. Chang, and R. Richards-Kortum, "Reflectance spectroscopy for diagnosis of epithelial precancer: model-based analysis of fiber-optic probe designs to resolve spectral information from epithelium and stroma," *Appl. Opt.* **44**(20), 4291–4305 (2005).
28. L. Nieman, A. Myakov, J. Aaron, and K. Sokolov, "Optical sectioning using a fiber probe with an angled illumination-collection geometry: evaluation in engineered tissue phantoms," *Appl. Opt.* **43**(6), 1308–1319 (2004).
29. A. Wang, J. Bender, J. Pfefer, U. Utzinger, and R. A. Drezek, "Depth-sensitive reflectance measurements using obliquely oriented fiber probes," *J. Biomed. Opt.* **10**(4), 044017 (2005).
30. M. Skala, G. Palmer, C. Zhu, Q. Liu, K. Vrotsos, C. Marshek-Stone, A. Gendron-Fitzpatrick, and N. Ramanujam, "Investigation of fiber-optic probe designs for optical spectroscopic diagnosis of epithelial pre-cancers," *Lasers Surg. Med.* **34**, 25–38 (2004).

31. R. A. Schwarz, D. Arifler, S. K. Chang, I. Pavlova, I. A. Hussain, V. Mack, B. Knight, and R. Richards-Kortum, "Ball lens coupled fiber-optic probe for depth resolved spectroscopy of epithelial tissue," *Opt. Lett.* **30**(10), 1151–1161 (2005).

32. C. K. Brookner, M. Follen, I. Boiko, J. Galvan, S. Thomsen, A. Malpica, S. Suzuki, R. Lota, and R. Richards-Kortum, "Autofluorescence patterns in short-term cultures of normal cervical tissue," *Photochem. Photobiol.* **71**, 730–736 (2000).

33. T. Collier, P. Shen, B. de Pradier, K. B. Sung, and R. Richards-Kortum, "Near real time confocal microscopy of amelanotic tissue: dynamics of aceto-whitening enable nuclear segmentation," *Opt. Express* **6**(2), 40–48 (2000).

34. S. Chang, D. Arifler, R. Drezek, M. Follen, and R. Richards-Kortum, "Analytical model to describe fluorescence spectra of normal and preneoplastic epithelial tissue: comparison with Monte Carlo simulations and clinical measurements," *J. Biomed. Opt.* **9**(3), 511–522 (2004).

35. K. W. Gossage, C. M. Smith, E. M. Kanter, L. P. Hariri, A. L. Stone, J. J. Rodriguez, S. K. Williams, and J. K. Barton, "Texture analysis of speckle in optical coherence tomography images of tissue phantoms," *Phys. Med. Biol.*, **51**, 1563–1575 (2006).

36. V. Backman, V. Gopal, M. Kalashnikov, K. Badizadegan, R. Gurjar, A. Wax, I. Georgakoudi, M. Mueller, C. Boone, R. Dasari, and M. Feld, "Measuring cellular structure at submicrometer scale with light scattering spectroscopy," *IEEE J. Quantum Electron.* **7**(6), 887–893 (2001).

37. V. Backman, M. Wallace, L. Perelman, J. Arendt, R. Gurjar, M. Muller, Q. Zhang, G. Zonios, E. Kline, T. McGillican, S. Shapshay, T. Valdez, K. Badizadegan, J. Crawford, M. Fitzmaurice, S. Kabani, H. Levin, M. Seiler, R. Dasari, I. Itzkan, J. Van Dam, and M. Feld, "Detection of preinvasive cancer cells," *Nature (London)* **406**, 35–36 (2000).

38. V. Backman, R. Gurjar, K. Badizadegan, I. Itzkan, R. Dasari, L. Perelman, and M. Feld, "Polarized light scattering spectroscopy for quantitative measurements of epithelial cellular structures *in situ*," *IEEE J. Sel. Top. Quantum Electron.* **5**, 1019–1026 (1999).

39. R. Gurjar, V. Backman, L. Perelman, I. Georgakoudi, K. Badizadegan, I. Itzkan, R. Dasari, and M. Feld, "Imaging human epithelial properties with polarized light-scattering spectroscopy," *Nat. Med.* **7**(11), 1245–1248 (2001).

40. K. J. Heppner, L. M. Matrisian, R. A. Jensen, and W. H. Rodgers, "Expression of most matrix metalloproteinase family members in breast cancer represents a tumor-induced host response," *Am. J. Pathol.* **149**, 273–282 (1996).

41. W. C. Parks, *Matrix Metalloproteinases*, Academic, San Diego (1998).

42. I. Pavlova, K. Sokolov, R. Drezek, A. Malpica, M. Follen, and R. Richards-Kortum, "Microanatomical and biochemical origins of normal and precancerous cervical autofluorescence using laser-scanning fluorescence confocal microscopy," *Photochem. Photobiol.* **77**, 550–555 (2003).

43. I. Georgakoudi, E. Sheets, M. Müller, V. Backman, C. Crum, K. Badizadegan, R. Dasari, and M. Feld, "Trimodal spectroscopy for the detection and characterization of cervical percancers *in vivo*," *Am. J. Obstet. Gynecol.* **186**, 374–382 (2002).

44. M. Müller, T. Valdez, I. Georgakoudi, V. Backman, C. Fuentes, S. Kabani, N. Laver, Z. Wang, C. Boone, R. Dasari, S. Shapshay, and M. Feld, "Spectroscopic detection and evaluation of morphologic and biochemical changes in early human oral carcinoma," *Cancer* **97**, 1681–1692 (2003).

45. P. Ravazoula, V. Zolota, O. Hatjicondi, G. Sakellaropoulos, G. Kourounis, and M. E. Maragoudakis, "Assessment of angiogenesis in human cervical lesions," *Anticancer Res.* **16**, 3861–3864 (1996).

46. J. S. Lee, H. S. Kim, J. J. Jung, M. C. Lee, and C. S. Park, "Angiogenesis, cell proliferation and apoptosis in progression of cervical neoplasia," *Anal Quant Cytol. Histol.* **24**, 103–113 (2002).

47. R. Hunter, M. Patterson, T. Farrell, and J. Hayward, "Haemoglobin oxygenation of a two-layer tissue-simulating phantom from time-resolved reflectance: effect of top layer thickness," *Phys. Med. Biol.* **47**, 193–208 (2002).

48. S. Bartel and A. Hielscher, "Monte Carlo simulations of the diffuse backscattering Mueller matrix for highly scattering media," *Appl. Opt.* **39**, 1580–1588 (2000).

49. X. Wang, G. Yao, and L. Wang, "Monte Carlo model and light-scattering approximation of the propagation of polarized light in turbid media containing glucose," *Appl. Opt.* **41**, 792–801 (2002).

50. Q. Liu, C. Zhu, and N. Ramanujam, "Experimental validation of Monte Carlo modeling of fluorescence in tissue in the UV-visible spectrum," *J. Biomed. Opt.* **8**, 223–235 (2003).

51. L. Wang, S. Jacques, and L. Zheng, "Monte Carlo modeling of light transport in multi-layered tissue," *Comput. Methods Programs Biomed.* **47**, 131–146 (1995).

52. Flock, M. Patterson, B. Wilson, and D. Wyman, "Monte Carlo modeling of light propagation in highly scattering tissues: model predictions and comparison with diffusion theory," *IEEE Trans. Biomed. Eng.* **36**, 1162–1173 (1989).

53. A. Welch, C. Gardner, R. Richards-Kortum, E. Chan, G. Criswell, T. J. Pfefer, and S. Warren, "Propagation of fluorescent light," *Lasers Surg. Med.* **21**, 166–178 (1997).